Supplementary Materials for

Data-Driven De Novo Design of Super-Adhesive Hydrogels

Hongguang Liao†, Sheng Hu†, Hu Yang, Lei Wang, Shinya Tanaka, Ichigaku Takigawa*, Wei Li*, Hailong Fan*, Jian Ping Gong*

Corresponding author: takigawa@icredd.hokudai.ac.jp; liw@szlab.ac.cn; fanhl@szu.edu.cn; gong@sci.hokudai.ac.jp

The PDF file includes:

Other Supplementary Materials for this manuscript include the following:

Materials

2-(Acryloyloxy)ethyl trimethyl ammonium chloride (ATAC, 79.4% in water) was provided by MT AquaPolymer, Inc. 2-Phenoxyethyl acrylate (PEA) was provided by Osaka Organic Chemical Co., Ltd., Japan. Butyl acrylate (BA) and 2-hydroxyethyl acrylate (HEA) were purchased from Tokyo Chemical Industry Co., Ltd. 2-Carboxyethyl acrylate (CBEA) and glycerol 1,3-diglycerolate diacrylate (GDD) were purchased from Sigma-Aldrich Co., Ltd. Acrylamide (AAm), 2-oxoglutaric acid, sodium chloride (NaCl), dimethyl sulfoxide (DMSO), and dimethyl sulfate (DMS) were purchased from Wako Pure Chemical Industries, Ltd. All chemicals were used as received without further purification. Millipore deionized water was used in all experiments.

Substrates for adhesion testing included commercially available glass (Matsunami Glass, Osaka, Japan, S2112), positively charged glass (MAS-coated Superfrost, Matsunami Glass, Osaka, Japan, S9441), stainless steel (SS), aluminum alloy (Al), titanium alloy (Ti), polyoxymethylene (POM), phenol formaldehyde (PF), polycarbonate (PC), polypropylene (PP), polytetrafluoroethylene (PTFE), and poly(methyl methacrylate) (PMMA). All substrates were rinsed with ethanol and then with deionized water before use.

Reactivity Ratio Measurement

Reactivity ratios of monomer pairs were determined by measuring monomer conversion kinetics during free-radical copolymerization at a concentration comparable to gel synthesis using ^{1}H NMR spectroscopy (Agilent 500 MHz)[28]. DMSO solutions containing a total of 1.0 M monomers with varying monomer ratios for the corresponding monomer pairs, along with 0.25 mol% UV initiator (2-oxoglutaric acid, in a concentration relative to the total monomer concentration), were prepared. Polymerization was carried out under UV light irradiation (3.9 mW cm^{-2}) inside a glove box. At different reaction times, 150 μL of the reaction mixture was withdrawn from the reaction solution tube, removed from the glove box, and exposed to air to quench the reaction. Subsequently, 300 μL of DMSO-d_6 was added into the sample for NMR analysis. The concentration of unreacted monomers was determined by comparing the integration of the double bond protons of residual monomers to the integration of aromatic protons from both residual monomers and formed copolymers. Reactivity ratios were calculated using the Mayo-Lewis equation[52].

Monte Carlo Simulations

Monte Carlo simulations were performed using the Compositional Drift program[31]. Unless otherwise specified, the statistical results presented are based on sequences generated by simulations involving 2 million monomers, with an average chain length of 100 and 100% conversion. The simulations were conducted using the gel formulations (Supplementary Tables 2 and 7) and the measured pairwise reactivity ratios of functional monomers (Supplementary Table 3). Simulations with different average chain lengths (up to 1,000) were also tested, showing only marginal differences in results.

Hydrogel Fabrication

Copolymer gels were synthesized via one-step free-radical copolymerization of functional monomers in the presence of a chemical crosslinker. The crosslinker concentration was fixed at 0.1 mol% relative to the total monomer content to balance the elasticity and deformability of the gels[28]. Solutions in DMSO containing functional monomers (total monomer concentration of 2.4 M) with compositions derived from data mining and machine learning (Supplementary Tables 2 and 7), GDD as the chemical crosslinker (2.4 mM), and 2-oxoglutaric acid as the UV initiator (6 mM) were used. For example, to prepare the G-max gel, a 10 mL volumetric flask was charged with 1.819 g of BA, 0.413 g of HEA, 0.264 g of CBEA, 0.561 g of ATAC, 0.441 g of PEA, 8.4 mg of GDD, and 8.8 mg of 2-oxoglutaric acid, then filled to volume with DMSO.

The precursor solution was transferred into a glove box to remove oxygen, poured into a reaction cell consisting of a pair of glass plates (10 cm × 10 cm, 0.5 mm spacing), and irradiated with UV light (365 nm wavelength, 4 mW cm^{-2} intensity) for 8 hours to form organogels (Supplementary Fig. 9a). After UV irradiation, over 99% monomer conversion to polymers was confirmed by ^{1}H NMR (Supplementary Fig. 9b). The as-prepared organogels were immersed in excess normal saline (0.154 M NaCl) to remove residual solvent and unreacted species, with the saline exchanged every 12 hours for at least two weeks until equilibrium was reached. The resulting hydrogels were stored in normal saline prior to use.

Hydrogel Mechanical Property Characterization

The volume swelling ratio (Q) was defined as the ratio of the hydrogel volume at swelling equilibrium in normal saline (V) to that in the as-prepared state (V_0), expressed as $Q = V/V_0$. Assuming isotropic swelling, thickness in the as-prepared state (d_0) and at swelling equilibrium (d) was measured using a thickness gauge (SDA-25, Kobunshi Keiki Co., Ltd.), and Q was

calculated as $Q = (d/d_0)^3$.

Rheological measurements were performed using an ARES-G2 rheometer (TA Instruments) in parallel-plate geometry at 24 °C. Hydrogels equilibrated in normal saline were cut into 15 mm diameter discs using a custom punch cutter. Samples were placed directly onto the plates, leveraging their inherent adhesion to avoid the need for additional adhesives. Frequency sweep tests were conducted at a shear strain of 0.1%, with angular frequencies ranging from 0.1 to 100 rad s^{-1}.

Uniaxial tensile test was performed on dumbbell-shaped specimens (JIS-K6251-7 size: gauge length = 12 mm, width = 2 mm), cut using a custom punch cutter. Measurements were carried out in air using a universal testing machine (UTM, Instron 5965) at a constant extension rate of 100 mm min^{-1}.

Pure shear tests were conducted to measure fracture energy (Γ)[53]. Two samples were prepared: one with a single edge notch and one without, both cut into rectangles (35 mm × 50 mm) using a custom punch cutter. Samples were clamped along their long edges with a grip height (H) of 10 mm. A 10 mm notch was introduced into one sample, which was stretched at 100 mm min^{-1} until crack propagation occurred at the critical stretch ratio (λ_c), monitored via video observation. The unnotched sample was stretched to the same λ_c, and the nominal stress (σ) was recorded as a function of the stretch (λ). The fracture energy was calculated from the stress-stretch ratio curve using $\Gamma = H \int_1^{\lambda_c} \sigma \mathrm{d}\lambda$.

All measurements were performed at least three times to obtain statistical results.

Histopathological Study

Histological examinations of wound healing were conducted under the dorsal skin of mature female Jcl:ICR mice, with an average weight of 20 g. Prior to surgery, dorsal fur was shaved, and mice were anesthetized using isoflurane. Incision surgery was performed to implant 6 mm round hydrogel samples within the connective tissue, and surgical sutures were used to secure the hydrogels in place. After surgery, the mice were allowed free movement and access to solid food and water in their cages.

Tissue samples in contact with the hydrogel were collected on days 7 and 14 for histopathological analysis. All specimens were fixed in a 4% paraformaldehyde solution for 2-3 days. The samples were embedded in paraffin, and tissue sections measuring 3-4 μm in thickness were prepared. Representative sections were stained with hematoxylin and eosin (H&E) for observation under light microscopy. For the control groups, incisions were made at

the corresponding sites on separate mice, and injured tissue sections without hydrogel contact were used for histopathological analysis. Each group included two mice, with one serving as the control. Following the experiments, all mice were euthanized.

The animal studies were conducted according to the protocol approved by the Institutional Animal Care and Use Committee at Hokkaido University WPI-ICReDD.

Supplementary Figures and Tables

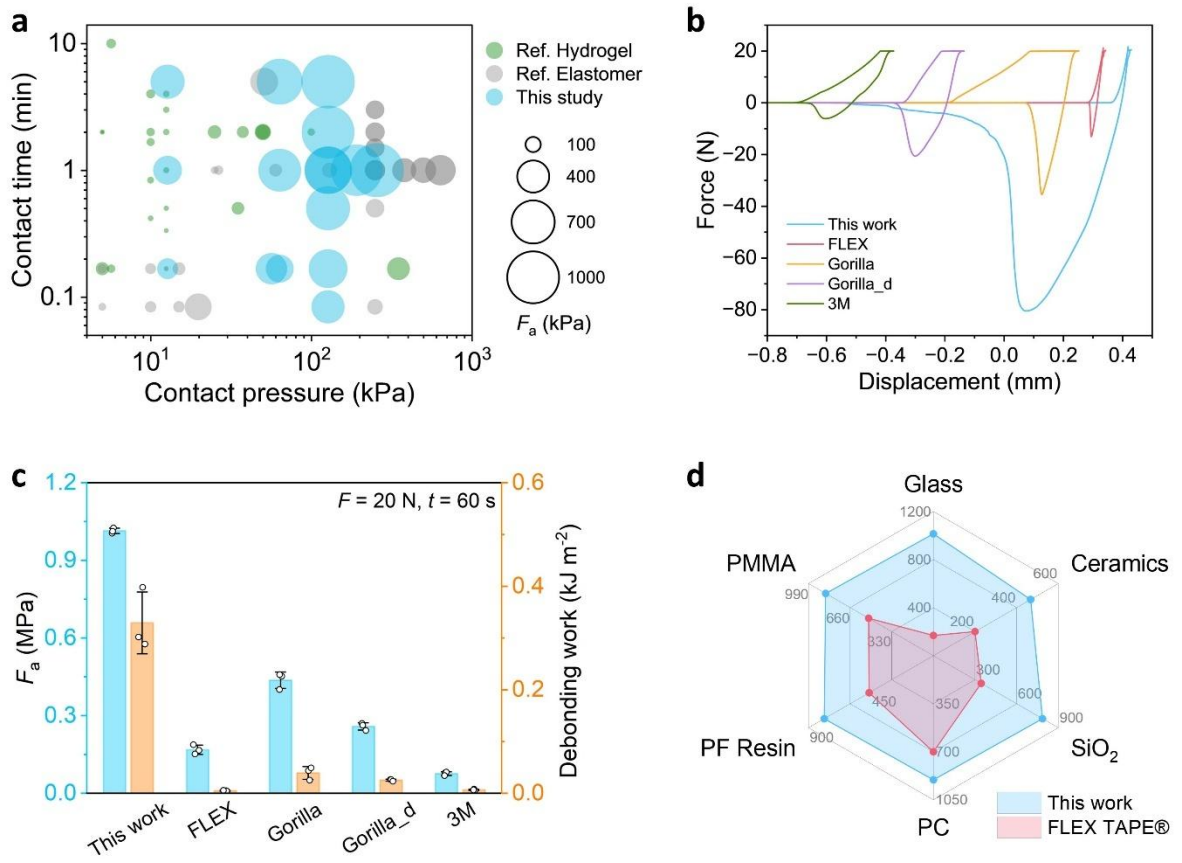

Supplementary Fig. 1. Comparison of adhesive performances between the R1-max hydrogel and literature/commercial tapes. (a) Comparison of adhesive strength (F_a) between a top-performing ML-driven hydrogel (R1-max) and tape-type adhesives from the literature, measured by tack tests at different contact pressures and times in various aqueous environments, following the setups described in the literature (see details in Supplementary Table 1). Symbol size represents the magnitude of F_a. (b) Force-displacement curves from tack tests (20 N loading force, 60 s contact time) assessing adhesion to a glass substrate in normal saline (0.154 M NaCl). Commercial tapes tested: FLEX TAPE® (super strong waterproof tape), Gorilla TAPE® (extreme waterproof seal & repair tape), Gorilla_d TAPE® (weatherproof strong double-sided tape), and 3M TAPE® (waterproof double-sided tape). (c) F_a and debonding work calculated from the data in panel (b). (d) Comparison of underwater adhesive strength of R1-max and FLEX TAPE® on various substrates, including glass, ceramics, silicon wafer (SiO_2), polycarbonates (PC), phenol formaldehyde resin (PF), and poly(methyl methacrylate) (PMMA). Error bars represent the standard deviation of $N = 3$ measurements.

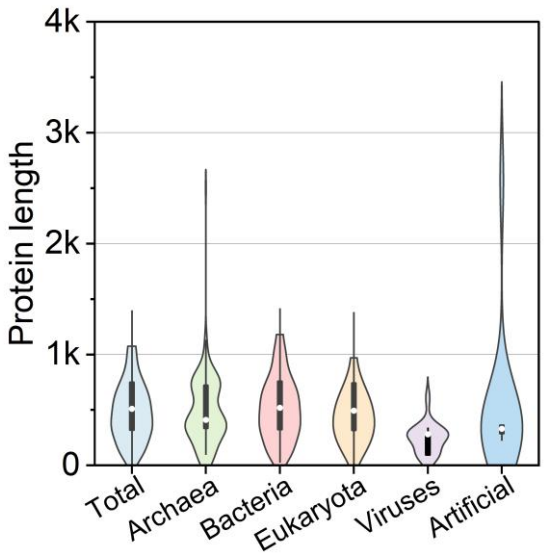

Supplementary Fig. 2. Violin plot showing the distributions of sequence lengths for adhesive proteins across the entire database (total) and within five biological categories.

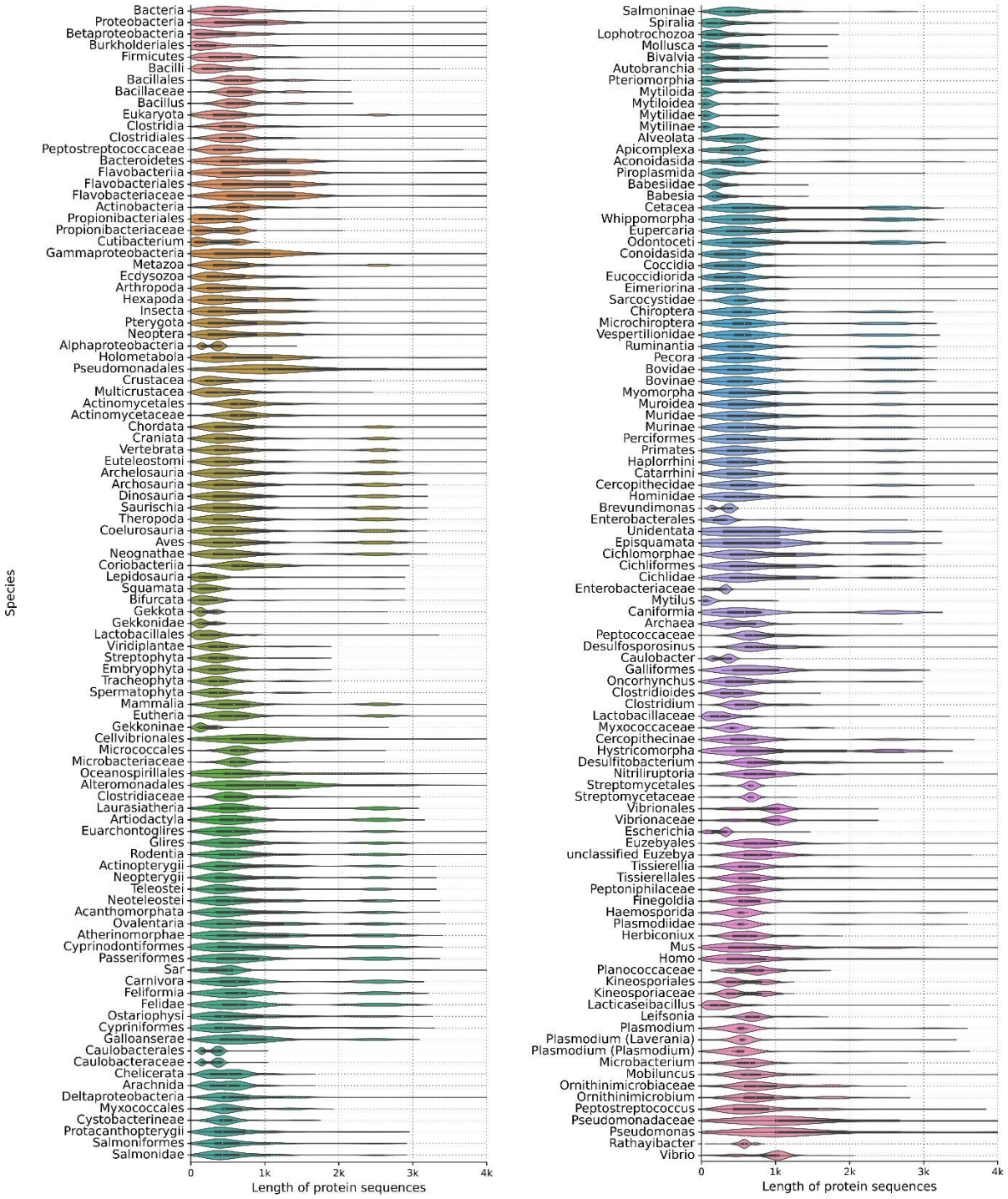

Supplementary Fig. 3. Violin plot showing the distributions of sequence lengths for adhesive proteins in the top 200 species, ranked by the number of adhesive proteins each has.

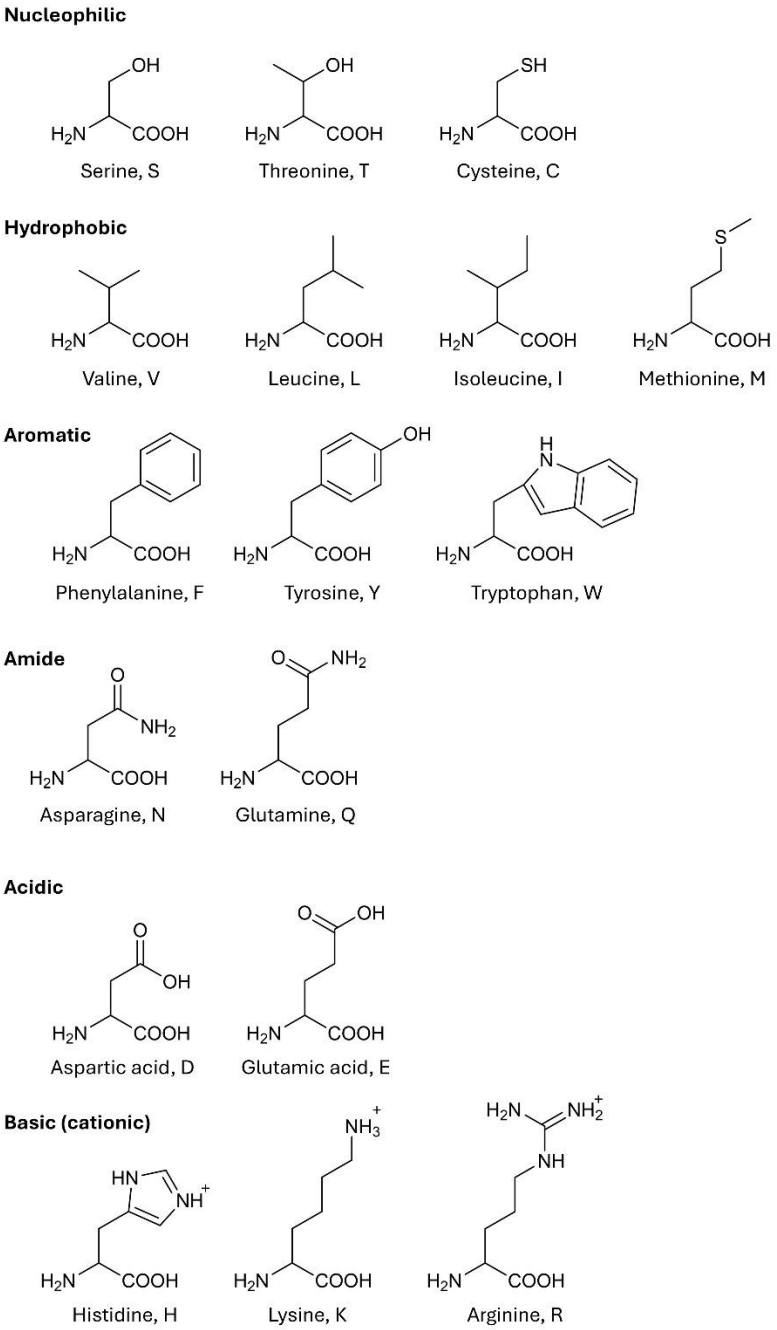

Supplementary Fig. 4. Classification of amino acids into six functional classes based on the physicochemical properties of their side chains.

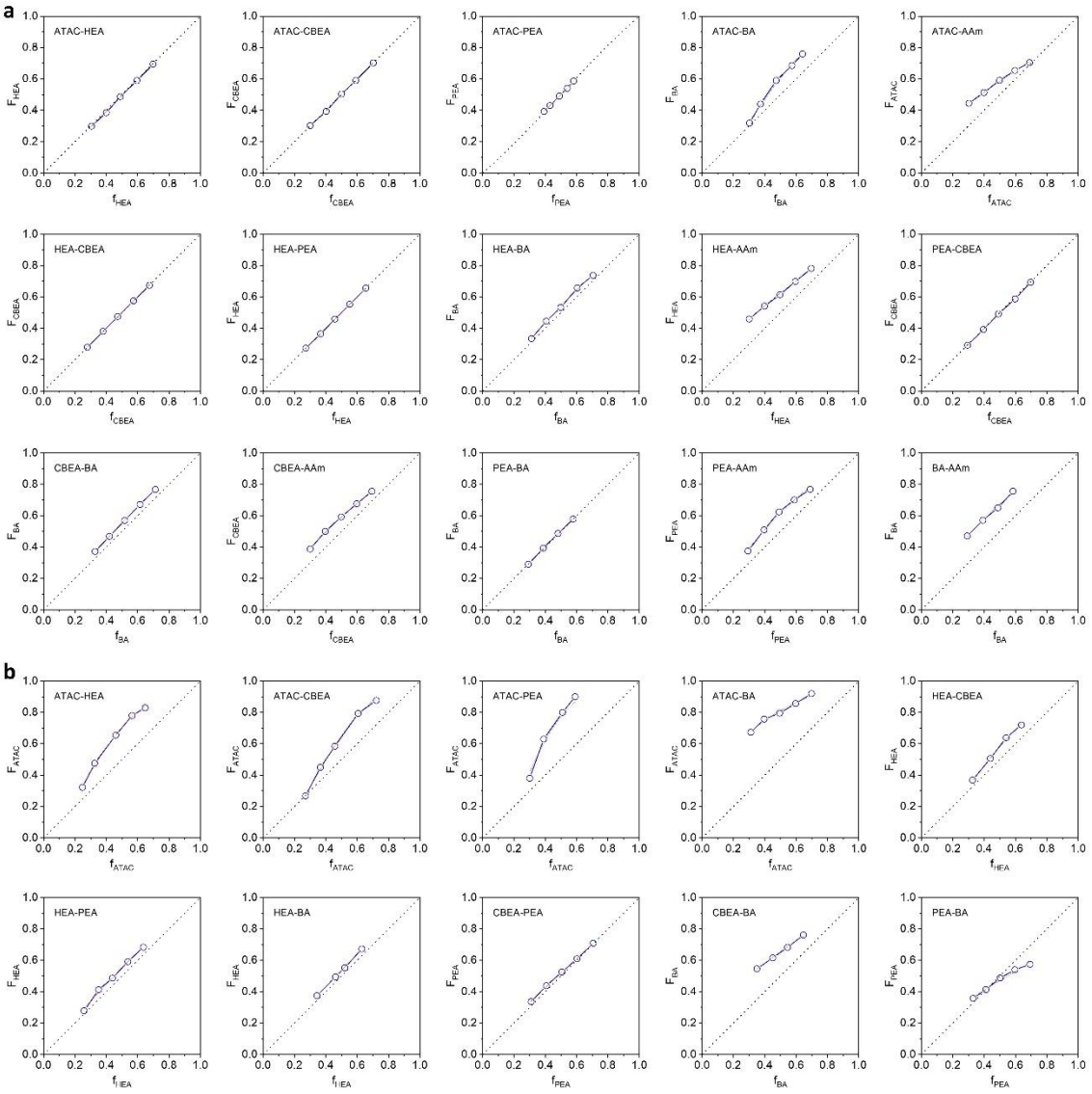

Supplementary Fig. 5. Monomer reactivity ratios in free radical copolymerization. Profiles of monomer mole fraction in copolymers (F_X) versus mole fraction in the feed (f_X), determined via ^{1}H NMR measurements, to estimate pairwise reactivity ratios of six functional monomers during free radical polymerization in different solvents. (a) DMSO and (b) DMS. The total monomer concentration was 1.0 M for each pair, and measurements were taken at monomer conversions below 10%. Experimental data (dots) were fitted using the Mayo-Lewis equation (red lines) to calculate reactivity ratios (r) for each monomer pair, as listed in Supplementary Table 3. Black dotted lines represent ideal random copolymerization. In DMSO, reactivity ratios range from 0.85 to 2.01, with most values close to 1, indicating quasi-ideal copolymerization. In DMS, reactivity ratios range from 0.25 to 20, showing significant deviation from ideal behavior.

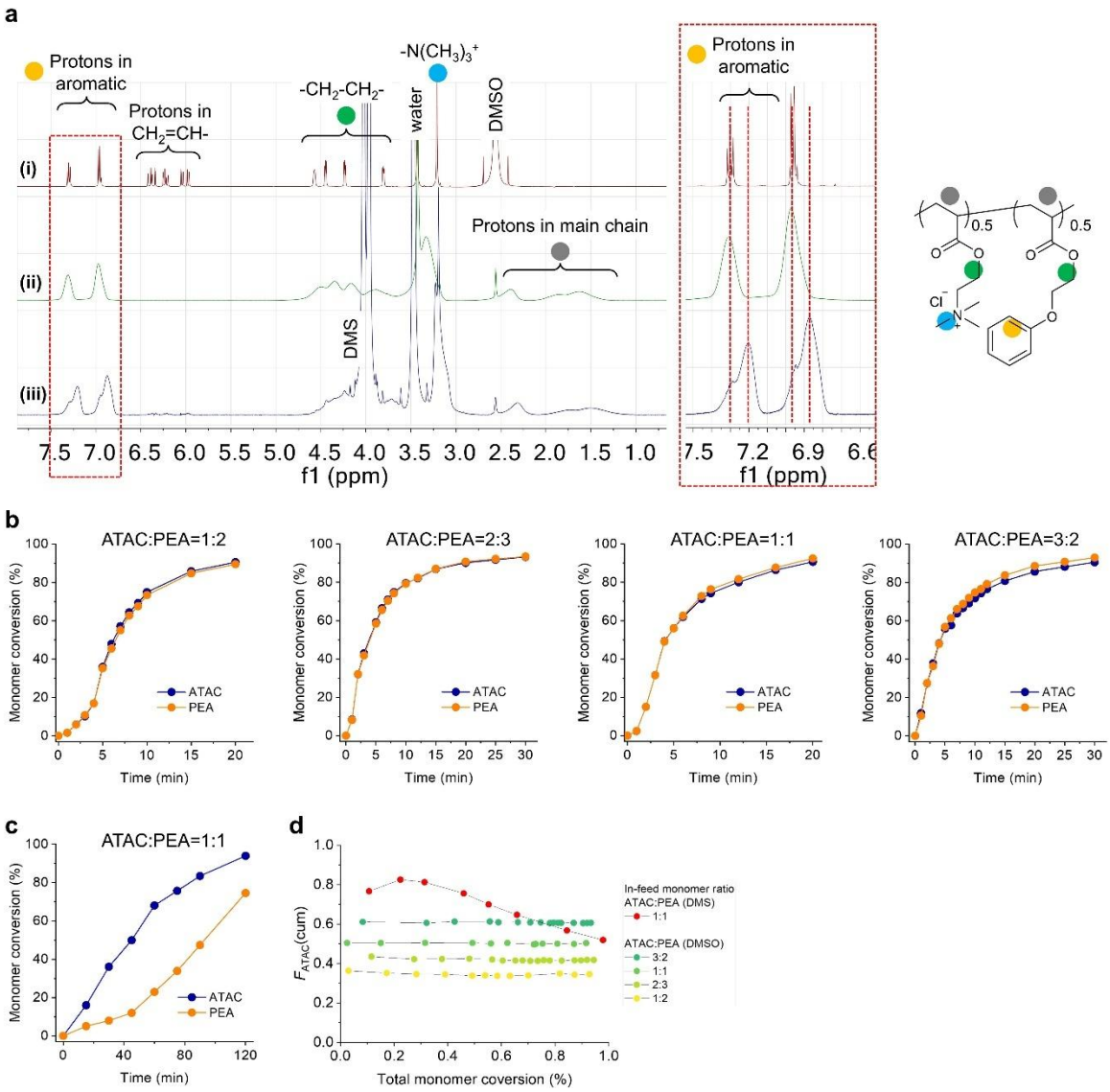

Supplementary Fig. 6. ^{1}H NMR analysis of copolymerization between cationic ATAC and aromatic PEA in different solvents. (a) ^{1}H NMR spectra of ATAC and PEA monomer precursor solutions at a 1:1 molar ratio (i) and of the corresponding copolymers after complete polymerization in DMSO (ii) and in DMS (iii). The region highlighted by a red dashed frame is enlarged on the right. For copolymers synthesized in DMSO, phenyl proton signals exhibit symmetric broadening around the peak of the phenyl protons of aromatic monomers, indicating a statistically random distribution of cationic and aromatic monomers along the copolymer chains. In contrast, copolymers synthesized in DMS show new, strong peaks at higher fields, suggesting the formation of long aromatic monomer sequences[41]. (b, c) Monomer conversion kinetics of ATAC and PEA at: (b) varying feed molar ratios in DMSO; and (c) a 1:1 feed molar ratio in DMS. (d) Cumulative ATAC molar fraction in the copolymers (F_{ATAC}) versus total monomer conversion for various feed molar ratios and solvents. In DMSO, copolymers maintained nearly the same monomer composition as the feed throughout polymerization, with

no significant composition drift, indicating quasi-ideal random copolymerization. In DMS at a 1:1 feed molar ratio, F_{ATAC} deviated significantly from 0.5 and varied with monomer conversion, demonstrating distinct composition drift during polymerization. In all experiments, the total monomer concentration was 1.0 M.

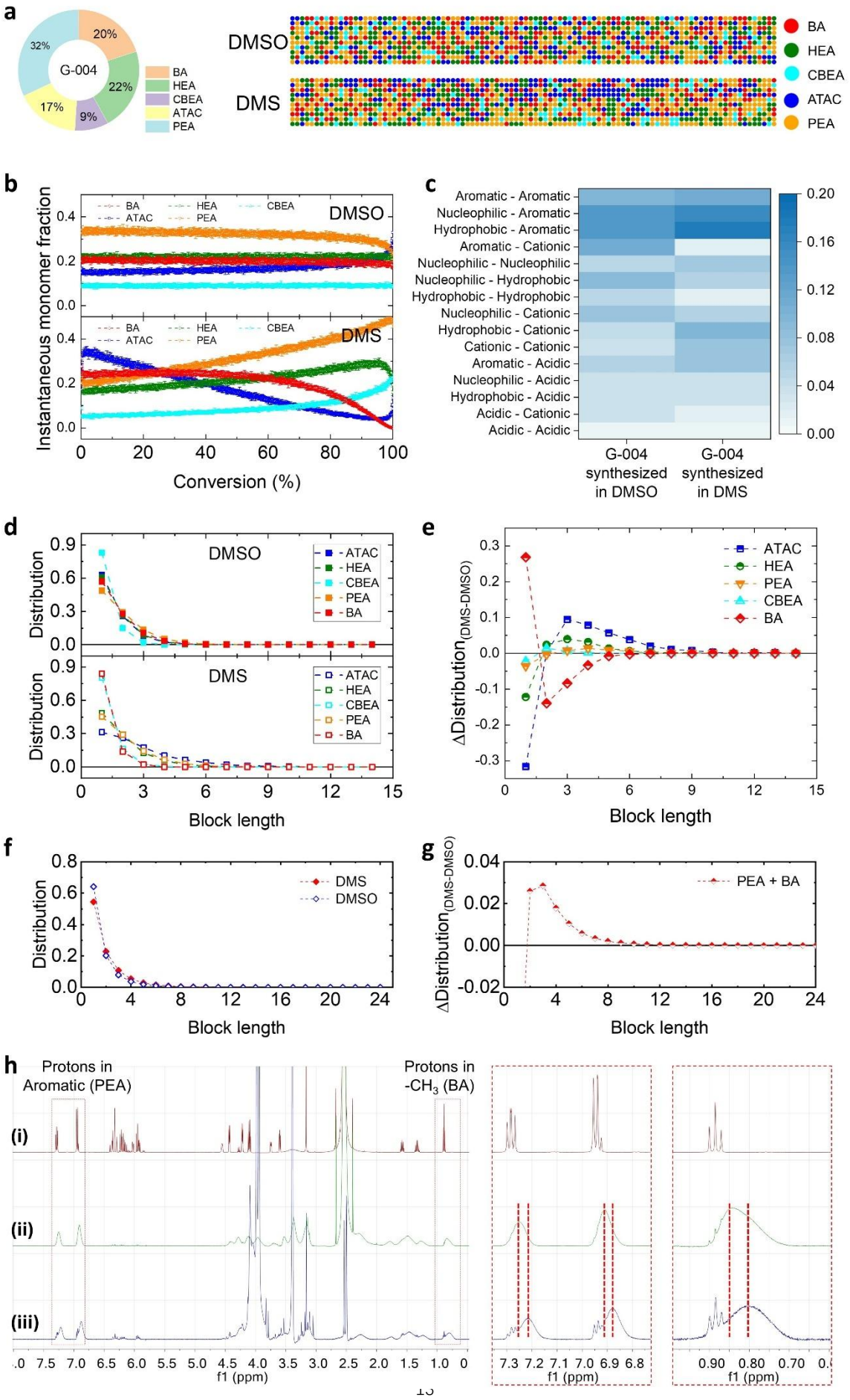
a
G-004
20%
22%
9%
17%
32%
BA
HEA
CBEA
ATAC
PEA
DMSO
DMS
b
Instantaneous monomer fraction
Conversion (%)
c
Aromatic - Aromatic
Nucleophilic - Aromatic
Hydrophobic - Aromatic
Aromatic - Cationic
Nucleophilic - Nucleophilic
Nucleophilic - Hydrophobic
Hydrophobic - Hydrophobic
Nucleophilic - Cationic
Hydrophobic - Cationic
Cationic - Cationic
Aromatic - Acidic
Nucleophilic - Acidic
Hydrophobic - Acidic
Acidic - Cationic
Acidic - Acidic
G-004 synthesized in DMSO
G-004 synthesized in DMS
d
Distribution
Block length
e
ΔDistribution(DMS-DMSO)
Block length
f
Distribution
Block length
g
ΔDistribution(DMS-DMSO)
PEA + BA
Block length
h
Protons in Aromatic (PEA)
Protons in -CH3 (BA)
(i)
(ii)
(iii)
f1 (ppm)

Supplementary Fig. 7. Monte Carlo simulations and ^{1}H NMR analysis of monomer sequences for G-004 prepared in DMSO and DMS. (a) G-004 formulation and simulated chain sequences in DMSO and DMS, based on reactivity ratios from Supplementary Table 3. Each chain consists of 1,000 monomers, presented in 10 rows of 100 monomers each, from left to right. (b) Instantaneous monomer fractions versus total monomer conversion during polymerizations in DMSO and DMS. Each simulation involved 2 million monomers, with an average chain length of 1,000. The results show minor composition drift for polymerization in DMSO, but significant composition drift in DMS throughout the polymerization. (c) Pairwise frequency distribution of 15 distinct functional class pairs along encoded sequences. (d) Block length distributions for different monomers from the simulated sequences. (e) Differences in monomer block length distributions between copolymers synthesized in DMS and DMSO, highlighting increased block lengths for ATAC, HEA, and PEA. (f) Block length distributions for combined aromatic PEA and hydrophobic BA in DMSO and DMS. (g) Difference between the two distribution curves in (f), suggesting longer segments of combined BA and PEA in DMS. Statistical results in (b-g) were obtained from five independent runs. (h) ^{1}H NMR spectra of G-004 monomer precursor solution (i) and copolymers synthesized in DMSO (ii) and in DMS (iii) after 8 hours of polymerization (conversion > 99% in DMSO and > 93% in DMS). Regions highlighted by red dashed frames are enlarged on the right. For PEA aromatic protons, a high-field shift in the peak indicates an increase in PEA block size. For BA methyl protons, a high-field shift suggests a higher frequency of adjacent BA-PEA units, corresponding to larger segments of combined BA and PEA monomers. These findings are consistent with the simulation results shown in (f, g). Overall, the simulations suggest that hydrogels prepared in DMSO exhibit quasi-ideal random copolymerization, yielding statistical monomer sequences that dictate the hydrogel's adhesion properties. In contrast, hydrogels prepared in DMS form blocky sequences of combined BA and PEA (both hydrophobic), which lead to aggregation of hydrophobic components and an opaque appearance (cf. Fig. 3f in the main text). Meanwhile, the increase in ATAC block length negatively impacts adhesion[1].

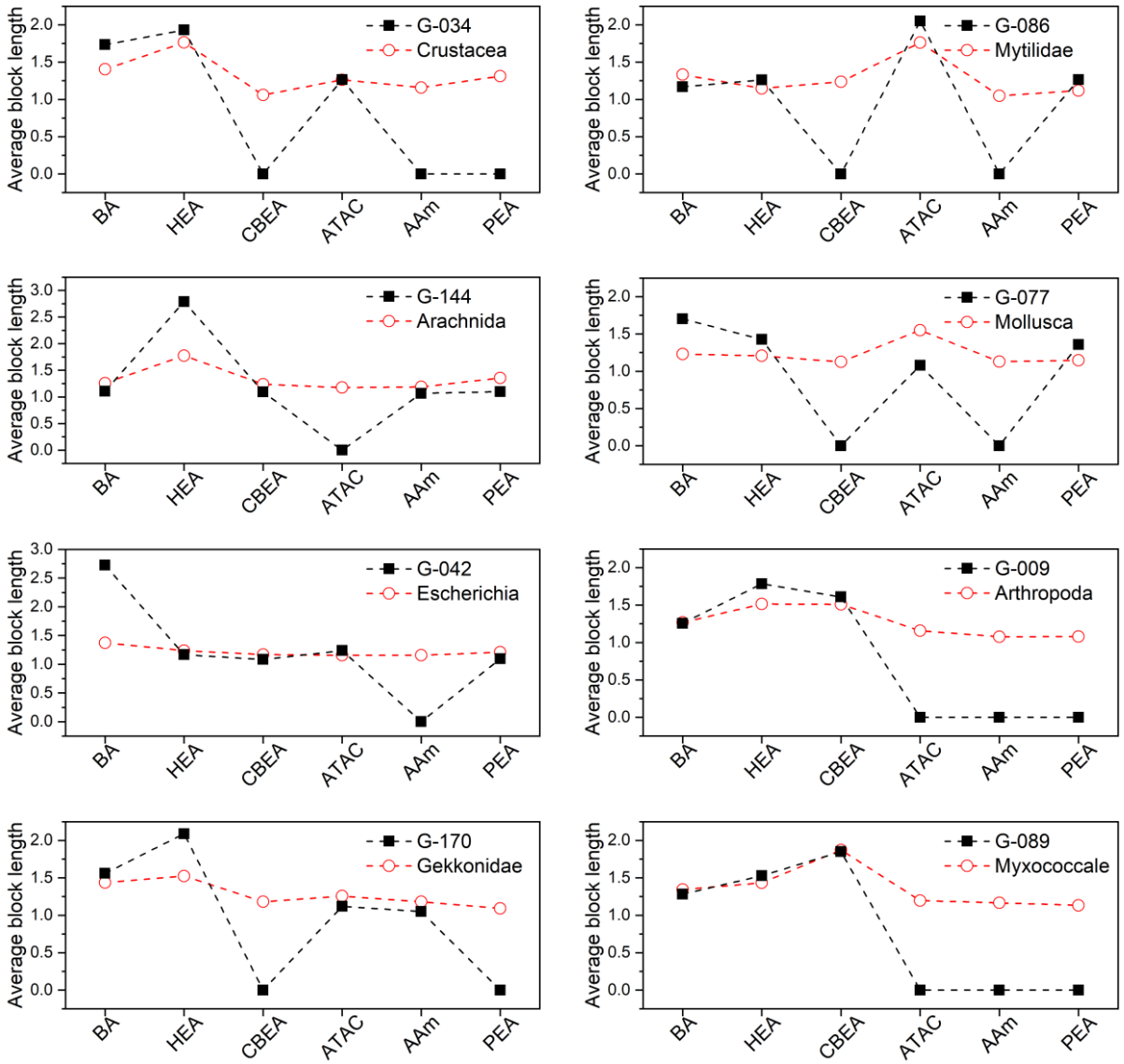

Supplementary Fig. 8. Comparison of average block lengths in hydrogel and biological sequences. Comparison of average block lengths between functional monomers, including BA (hydrophobic), HEA (nucleophilic), CBEA (acidic), ATAC (cationic), AAm (amide), and PEA (aromatic), in heteropolymer sequences (generated via Monte Carlo simulations) associated with the gel formulations in Fig. 3c and the functional classes in the consensus sequences of corresponding biological species in Fig. 2c of the main text. Due to the implementation of enhanced sampling (i.e., selecting the top five pairs from the pairwise frequency sorting), some functional monomers are absent from the extracted formulations. Nevertheless, the comparison shows reasonable agreement in average block lengths, providing another degree of statistical similarity in addition to pairwise frequency.

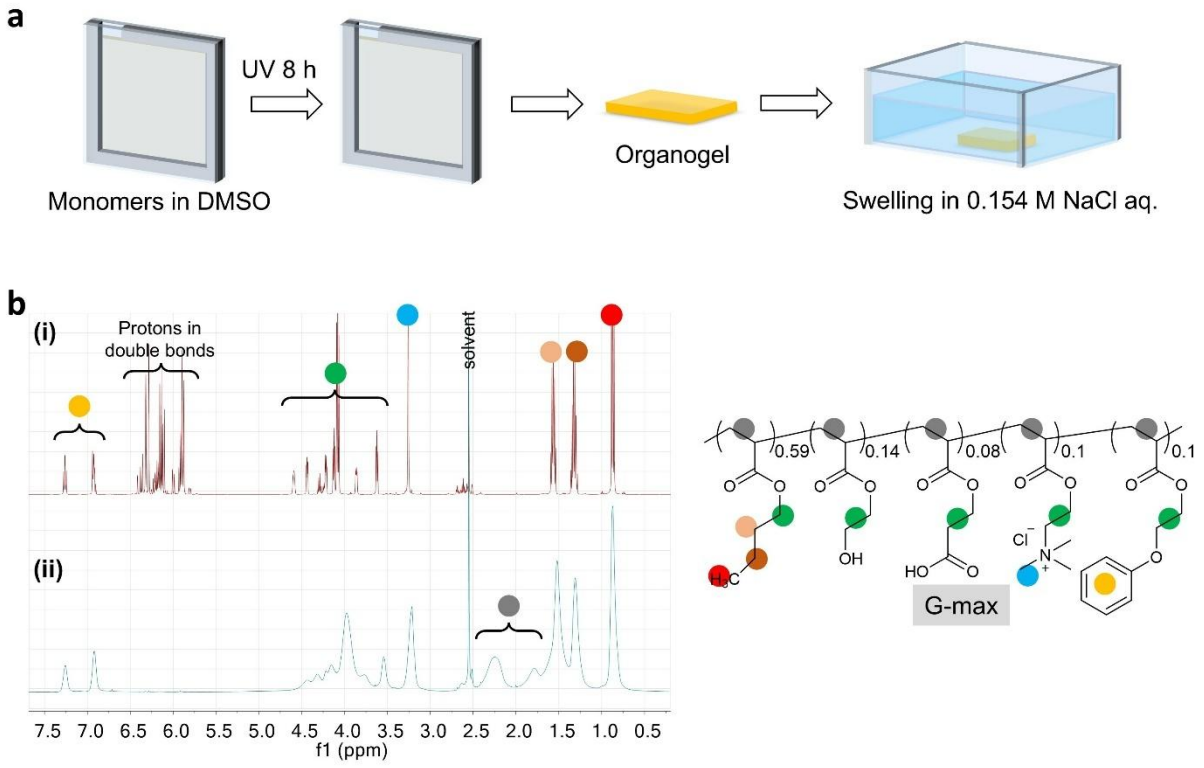

Supplementary Fig. 9. Hydrogel fabrication and characterization. (a) Schematic diagram illustrating the hydrogel fabrication procedure via free radical copolymerization. (b) ^{1}H NMR spectra of the monomer precursor solution for G-max (i) and the corresponding gel (ii) synthesized in DMSO. Based on the intensity of proton signals from double bonds, the monomer conversion ratio for gel formation was estimated to exceed 99%.

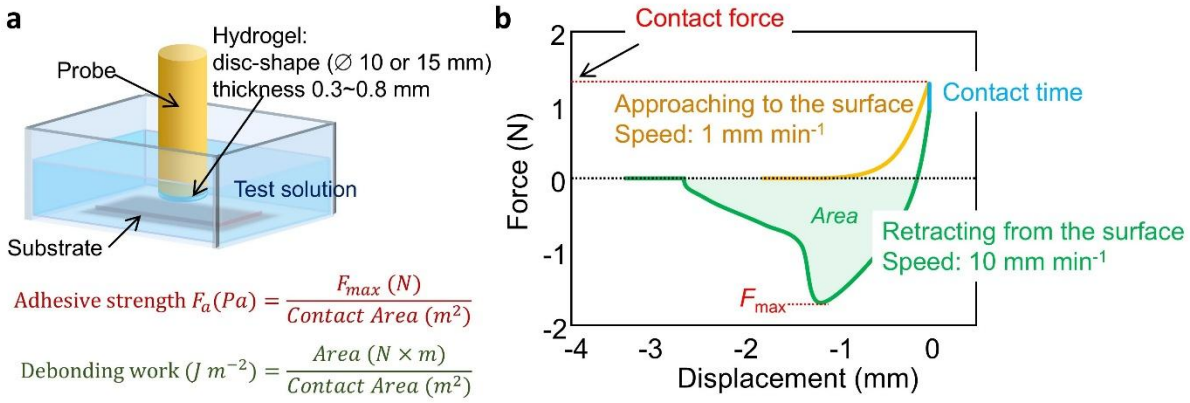

Supplementary Fig. 10. Schematic illustration of tack test for adhesion measurement. (a) Experimental setup for the tack test to measure gel adhesion in a liquid environment. (b) Illustration of the force-displacement curve with corresponding test parameters. The probe approach rate was set at a relatively low 1 mm min^{-1} to gradually increase the loading force.

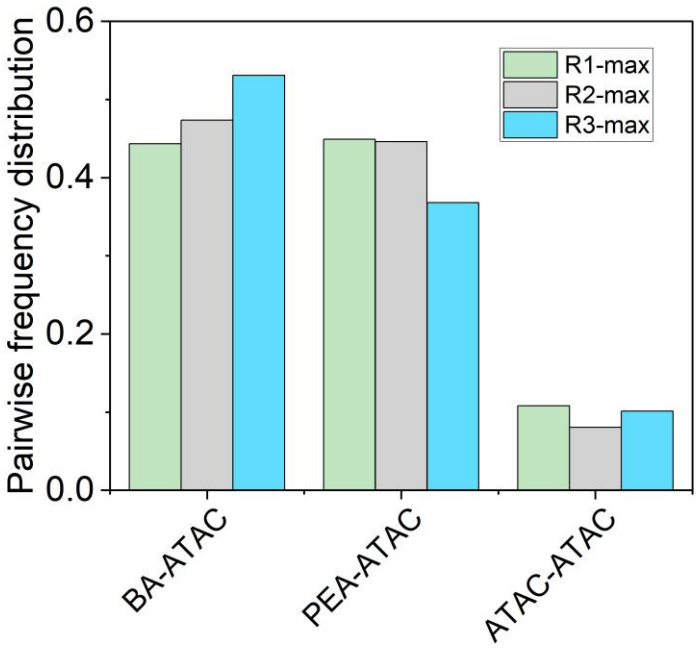

Supplementary Fig. 11. Pairwise frequency distribution of monomer pairs containing ATAC in copolymer sequences generated via Monte Carlo simulations using R1-max, R2-max, and R3-max formulations. The results reveal higher fractions of heterogeneous ATAC-containing pairs compared to the homogeneous ATAC-ATAC pair.

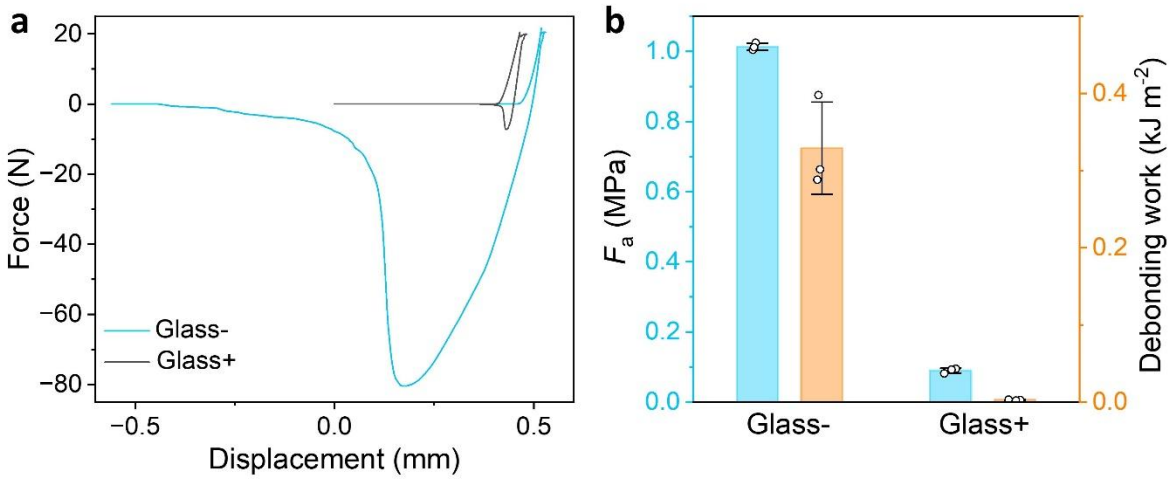

Supplementary Fig. 12. Influence of substrate surface charge on R1-max adhesion. (a) Force-displacement curves from tack tests of R1-max (10 mm diameter, ~0.4 mm thickness) on glass substrates with negatively and positively charged surfaces in normal saline (0.154 M NaCl), conducted under a 20 N loading force with 60-second contact time. (b) Extracted adhesive strength (F_a) and debonding work.

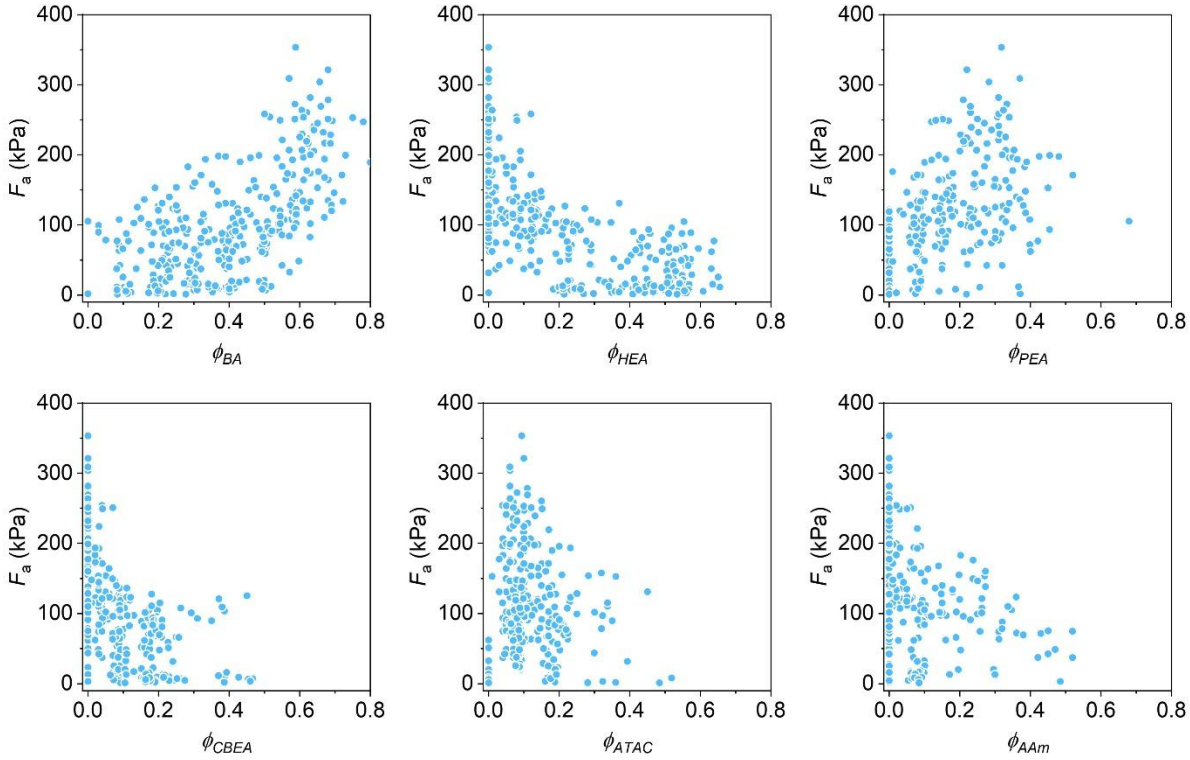

Supplementary Fig. 13. Adhesive strength (F_a) as a function of individual monomer proportions for all 341 hydrogel samples (see formulations in Supplementary Tables 2 and 7).

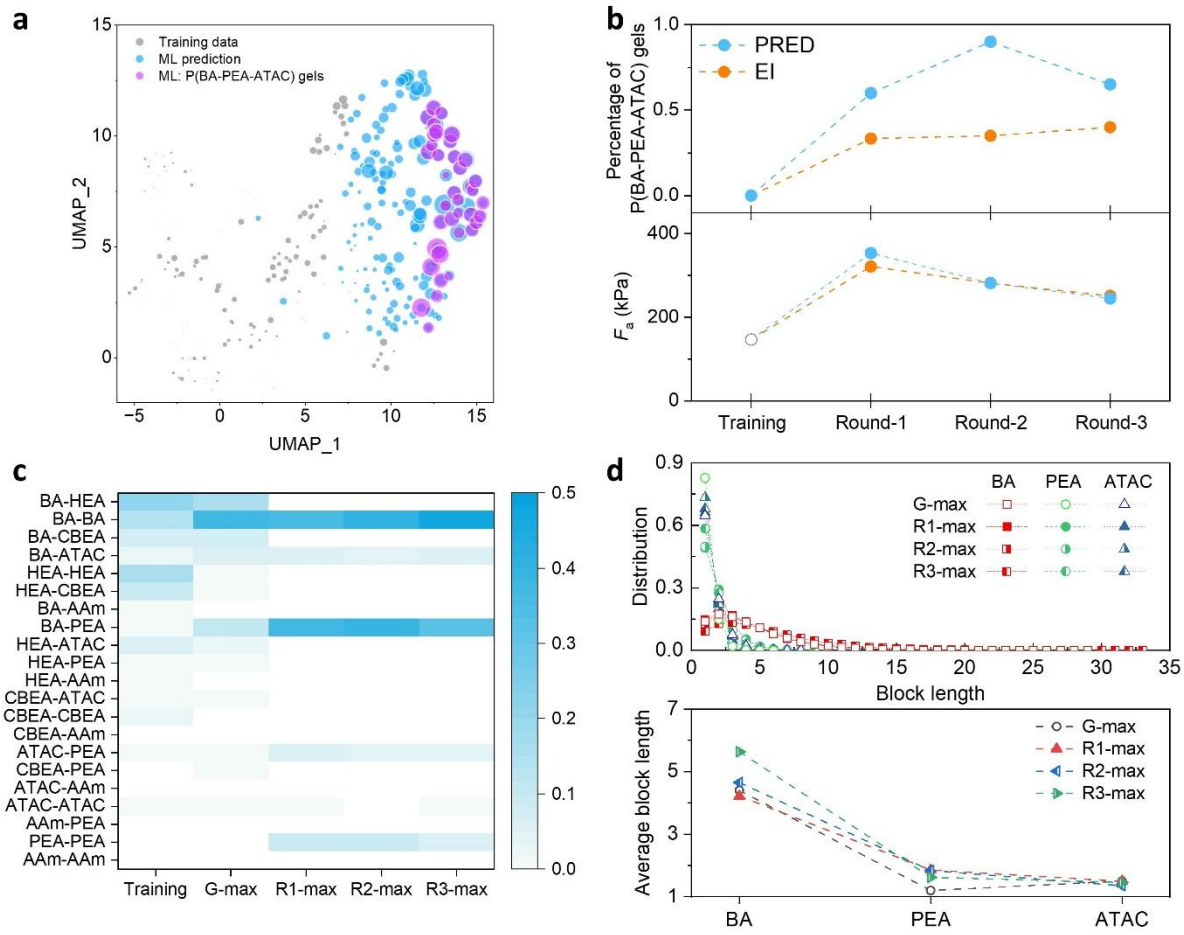

Supplementary Fig. 14. Properties of data mining-driven and machine learning-drive hydrogels. (a) UMAP representation of adhesive strength (F_a) versus reduced monomer proportions, highlighting the adhesive performance of ML-predicted three-component gels comprising BA, PEA, and ATAC, denoted as P(BA-PEA-ATAC) gels. The training dataset does not include this type of gels. (b) Percentage of three-component P(BA-PEA-ATAC) gels among tested gels, alongside the highest F_a values in the training and three ML optimization rounds, distinguishing results from the PRED and EI sorting schemes. In each ML optimization round, the gels with the highest F_a are all P(BA-PEA-ATAC) gels. (c) Pairwise frequency distribution of 21 functional class pairs in the entire training dataset of 180 hydrogels, the five-component G-max hydrogel, and the top-performing three-component ML-driven hydrogels, obtained from Monte Carlo simulations based on formulations and pairwise reactivity ratios. (d) Comparison of block length distributions and corresponding average block lengths for BA, PEA, and ATAC in the top-performing hydrogels, demonstrating similar statistical sequence features.

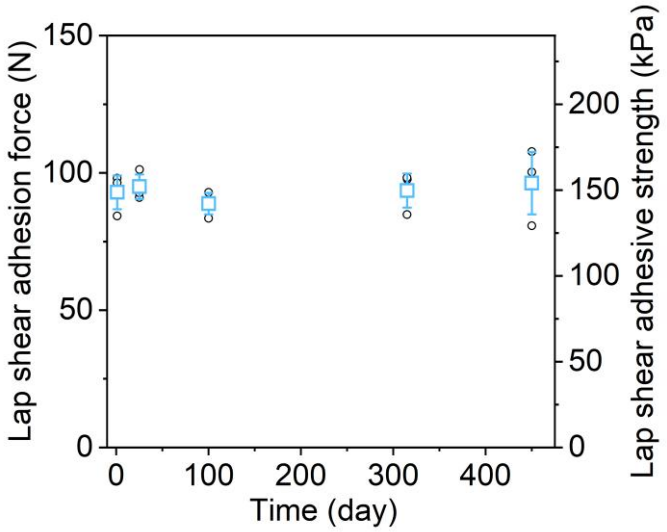

Supplementary Fig. 15. Adhesion of the R1-max hydrogel in lap shear geometry (joining two glass plates) as a function of days immersed in normal saline after sample preparation, demonstrating long-lasting adhesion. R1-max (25 × 25 mm^2, ~0.4 mm thickness) at its swelling equilibrium was sandwiched between two glass plates and compressed under a 20 N force for 1 minute in normal saline. More than 25 lap shear samples of this type were prepared and stored in normal saline without applying external compression force. The lap shear test was conducted at various time intervals. Lap shear adhesive strength was estimated by dividing the lap shear adhesion force by the joint area (25 × 25 mm^2). Error bars represent the standard deviation of $N = 3$ measurements.

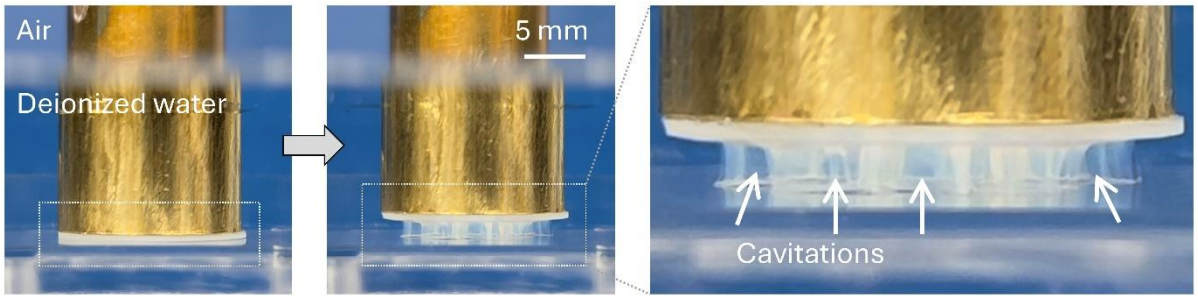

Supplementary Fig. 16. Photographic images illustrating the deformation of R2-max during retraction from a glass substrate in deionized water. Finger-like structures indicate cavitation caused by strong adhesion. Adhesion tests were conducted with a 10 N loading force applied for 10 seconds.

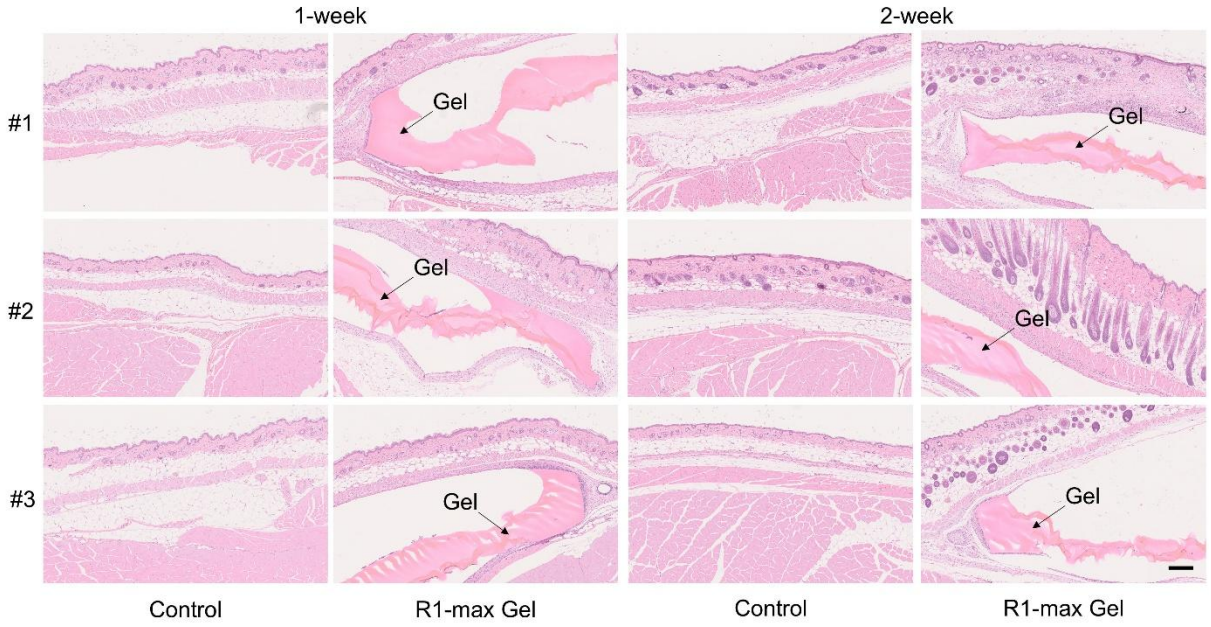

Supplementary Fig. 17. Histopathologic profiles of tissues in contact with the R1-max hydrogel over time. Normal mouse subcutaneous tissue is shown as a control. Hematoxylin and eosin (H&E) staining was used for examination. The scale bar represents 200 μm. During the first week, tissues in contact with the hydrogel showed a significant increase in fibroblasts and capillaries, accompanied by mild inflammatory cell infiltration. By the second week, the tissue layer above the granulation layer had thickened, with the thickness of the newly generated tissue in contact with the hydrogel exceeding that of the tissue not in contact with it. Mild inflammatory cell infiltration persisted. Throughout the healing process, minimal inflammatory cells (e.g., neutrophils, macrophages, and lymphocytes) were observed, indicating that minimal inflammation induced by the foreign hydrogel. These findings underscore the good biocompatibility and biological safety of the hydrogel *in vivo*.

Supplementary Algorithm 1: SMBO for the extrapolation of optimal monomer proportions.

Algorithm 1: SMBO for optimal monomer fraction extrapolation

Input : $f, \mathcal{X}, S, \mathcal{M}$

$D \leftarrow \mathsf{GetTrainingSet}(f, \mathcal{X})$; /* Obtain training data */

for $n = 1 \cdots T$ **do**

  $p(y \mid \mathbf{x}, D) \leftarrow \mathsf{FitModel}(\mathcal{M}, D)$;

  $\mathbf{x}_i \leftarrow \mathsf{SelectBestFractions}(S(\mathbf{x}, p(y \mid \mathbf{x}, D)))$;

  $y_i \leftarrow f(\mathbf{x}_i)$; /* Expensive evaluation */

  $D \leftarrow D \cup (\mathbf{x}_i, y_i)$;

return D;

Supplementary Table 1. Summary of tape-type underwater adhesives based on physical interactions, as reported in the literature and in this work.

Hydrogels						
Components	Substrates	Test method	Bonding condition Curing time	Adhesion strength	Remarks	Ref.
P(BA-stat-PEA-stat-ATAC)	Glass, ceramics, plastic, metals, bones	Tack test Lap shear 180° peel test	10 -120 s in water	500-1100 kPa 2.5-3 kJ m^{-2} (peel)	Reusable (200 cycles) Stable >1 year	**This work**
P(MATAC-co-AAm)	P(AAc) gel	Tack test	1-1200 s in water	10-20 kPa	-	54
P(AAm) + TA + Alg-Na	Glass, Al, plastic, tissue	Lap shear	Underwater	5-20 kPa	-	55
P(cation-adj-π)	Glass, metal, plastics, hydrogels	Tack test Lap shear	10 s in seawater	60 kPa	Reusable (16 cycles) Stable 14 d	28,41
P(cation-co-π_{rich})	Glass, metal, plastics	Tack test Lap shear	10 s in water	100-180 kPa	Reusable (50 cycles) Stable 100 d	56
P(AAc-co-MEA-co-Aa-co-AU)	Glass, metal, plastics	Lap shear	30 min	5-25 kPa	-	57
P(AAm-co-urushiol) + Glycerol	Glass	180° peel test Lap shear	2 min in water Then 30 min in air	200-400 J m^{-2} (peel) ~16 kPa (lap shear)	Antifreezing anti-heating	58
P(AAm-co-SMA) + SDS + Fe^{3+}	Glass, metal, plastics	Tack test	Wet surface 120 s	15-60 kPa	Reusable (50 cycles) Stable 15 d	59
P(C_{18}-co-DMAEMA-co-HEA) + SDS + Fe^{3+}	Glass, PE, steel, rubber	Lap shear	5-30 min	10-30 kPa	Reusable (10 cycles)	60
P(AAm-co-C_{18}) + PTA + Fe^{3+}	Glass, metal, plastics	Tack test	Wet surface 120 s	40-90 kPa	-	61
polydiolcitrates/P(GMA)	Glass, silica, metal, plastics	Tack test	0 s in water	50-100 kPa	Thermosensitive	62
HPMC/SiW-P(DMAEMA)/Fe^{3+}	Glass, metal, plastics	Lap shear	1 h in water	45-55 kPa	-	63
PEG-dA + TA	Glass, tissue	Tensile test Lap shear	In water	130 kPa (tensile) 22 kPa (lap shear)	-	64
PAH-catechol	Glass, tissue, PET	Lap shear	1 h in water	1.5-10 kPa	-	65
Polyampholyte	Glass, PS, PA, tissue	Tack test	10 s in water	12-27 kPa	Drainage	66
P(HEA-co-PEA-co-MEA) + MXene	Glass, metal, plastics, skin	Tack test	2 min in water	15-20 kPa	Reusable (5 cycles) Conductivity	67
P(SBVI) + graphene	Glass, metal, wood	Tack test	10 min in water	20-60 kPa	Conductivity	68
P(AAm-co-BI) + PCD	Al	Tack test	10 s in water	20 kPa	-	69
P(ATAC-co-EA) + TPP	PDMS	Tack test	30 s in water	55 kPa	-	70
P(AAc-co-BA)	Glass, metal, plastics	Lap shear Tack test	5 min	5-35 kPa	-	71
P(AAm-co-MAEDS) + P(LMA)	Glass, metal, plastics	Lap-shear	5 min-24 h In water	10-40 kPa	Phase separation gel	72
P(AAc) + QAX + TA	Glass, metal, plastics	Lap-shear	60 s in water	45-55 kPa	-	73
P(AAc-co-EHA)	Glass, metal, plastics, skin	Lap-shear	30 min in water	10-45 kPa	Reusable (15 cycles)	74
P(AAc-co-BA-ATAC) DMSO	Metal, plastics, skin	Lap-shear	In water	50-180 kPa	Solvent exchange	75
P(Aac-co-HEAA-co-MMA) + PANa	Metal, glass, wood, plastics, skin	Lap-shear	In water	5-20 kPa	Reusable (5 cycles)	76
P(MA-co-HGAc-co-HG-co-AAm/AAc)	Metal, glass, plastics, skin	Lap-shear	1 min in air then 12 h in water	3-30 kPa	Solvent exchange	77
P(C6-co-St-co-AAc-co-CD)	Metal, glass, plastics, skin	Lap-shear	30 min in water	20-100 kPa	Reusable (70 cycles)	78
P(AAc-co-PEA) + Chitosan	Skin	Lap-shear	30 s in water	4-60 kPa	-	79

Elastomers						
Components	Substrates	Test method	Bonding condition Curing time	Adhesion strength	Remarks	Ref.
P(PPO-co-GBC)	SS	Tack test 180° peel test	5 s	240 kPa 500 J m^{-2}	Thermal sensitive	80
P(MEA-co-ATU)	Glass, PS, Al, wood	Tack test	underwater	50-160 kPa	-	81
polydiolcitrates	Glass	Tack test	underwater	80 kPa	-	82
P(DMA-co-BA) + P(AAc-co-BA)-g-An	Glass, plastic	Tack test	10 s in water	15-60 kPa	Phototunable adhesion	83
P(BA-co-AAc)	Glass, plastic, metal	Tack test	60 s in water	120-150 kPa	Reusable (30 cycles)	84
P(IBOA-co-POFA)	Glass, plastic, metal	Tack test Lap shear	In water	75-180 kPa	Reusable (50 cycles) Stable 40 d	85
P(NVP-co-HPPA-co-C12A)	Glass, plastic, metal	Lap shear	In water	250-400 kPa	Reusable (10 cycles) Stable 15 d	86
TFMD	Glass, plastic, metal	Lap shear	20 min in water	900-1200 kPa	-	87
PDMS + TDCA + metal ions	Glass, plastic, metal	Tack test	60 s in water	5-35 kPa	Reusable (20 cycles)	88

Supplementary Table 2. (separate file) Formulations of 180 hydrogels derived from data mining analysis of adhesive proteins, along with their swelling and rheological properties in normal saline (0.154 M NaCl). Columns include: sample index, monomer proportions (ϕ_i), adhesive strength (F_a) measured by tack test on a glass substrate with a 10 N loading force and 10-second contact time, hydrogel thickness (d), volume swelling ratio (Q), storage modulus (G') at a frequency of 10^0 rad s^{-1}, loss factor ($Tan\ \delta$) at a frequency of 10^0 rad s^{-1}, and the slope (k) of the G'-frequency curve. The top-performing gel (G-042) is highlighted in bold.

Supplementary Table 3. Reactivity ratios (r_1 and r_2) between various pairs of functional monomers in DMSO and DMS.

Reactivity ratios in DMSO			
Monomer 1	Monomer 2	r_1	r_2
ATAC	HEA	1.06±0.03	1.01±0.04
ATAC	CBEA	1.00±0.04	1.00±0.04
ATAC	PEA	1.03±0.03	1.04±0.04
ATAC	BA	1.51±0.30	2.83±0.45
ATAC	AAm	0.82 ±0.04	0.29 ±0.02
HEA	CBEA	0.99±0.01	1.00±0.01
HEA	PEA	1.00±0.01	1.00±0.01
HEA	BA	0.95±0.06	1.29±0.08
HEA	AAm	1.30±0.06	0.37 ±0.03
CBEA	PEA	0.96±0.02	0.99±0.03
CBEA	BA	0.91±0.02	1.39±0.03
CBEA	AAm	1.32±0.05	0.60 ±0.03
PEA	BA	0.99±0.04	1.02±0.04
PEA	AAm	1.73±0.21	0.71±0.11
BA	AAm	2.01±0.24	0.45±0.08
Reactivity ratios in DMS			
Monomer 1	Monomer 2	r_1	r_2
ATAC	HEA	4.42±0.56	1.28±0.18
ATAC	CBEA	5.92±1.01	2.69±0.47
ATAC	PEA	20.0±3.2	5.11±0.87
ATAC	BA	4.01±0.48	0.16±0.06
HEA	CBEA	1.92±0.20	1.11±0.13
HEA	PEA	1.33±0.14	0.88±0.09
HEA	BA	0.94±0.06	1.25±0.07
CBEA	PEA	0.78±0.02	0.92±0.02
CBEA	BA	0.25±0.02	1.38±0.06
PEA	BA	0.33±0.05	0.50±0.06

Supplementary Table 4. Formulations of hydrogels derived from data mining analysis of resilin proteins, along with their volume swelling ratios (Q) and adhesive strength (F_a). Measurement was not feasible for gels r-03 to r-06 due to severe shrinkage and irregular shapes formed during solvent exchange. Tack tests were conducted under a 10 N loading force applied for 10 seconds on a glass substrate in normal saline. All hydrogels were equilibrated in normal saline (0.154 M NaCl).

No.	Φ_{HEA}	Φ_{BA}	Φ_{CBEA}	Φ_{ATAC}	Φ_{PEA}	Φ_{AAm}	Q	F_a (kPa)
r-01	0.333	0.358	0.000	0.083	0.227	0.000	0.81±0.02	59.55±1.09
r-02	0.324	0.058	0.000	0.000	0.160	0.458	0.50±0.02	18.23±0.42
r-03	0.324	0.388	0.100	0.000	0.188	0.000	No data	No data
r-04	0.337	0.376	0.100	0.000	0.187	0.000	No data	No data
r-05	0.193	0.471	0.144	0.000	0.192	0.000	No data	No data
r-06	0.519	0.189	0.000	0.000	0.198	0.094	0.42±0.02	19.99±2.88
r-07	0.510	0.194	0.105	0.000	0.192	0.000	0.55±0.00	25.24±0.06
r-08	0.394	0.000	0.357	0.000	0.184	0.065	0.36±0.01	10.17±2.94
r-09	0.526	0.180	0.000	0.072	0.221	0.000	0.73±0.00	36.98±2.45
r-10	0.585	0.092	0.123	0.000	0.120	0.080	0.48±0.03	9.23±0.20
r-11	0.257	0.372	0.000	0.000	0.309	0.062	0.24±0.00	10.73±1.20
r-12	0.591	0.125	0.000	0.095	0.098	0.091	1.51±0.04	42.42±6.60

Supplementary Table 5. Definitions of the regression models used in this work.

Type	Subcategory	Method	Description
Linear		Lasso	Performs linear regression with L1 regularization, leading to feature selection by shrinking some coefficients to zero.
		Ridge	A linear regression method with L2 regularization, which helps prevent overfitting by penalizing large coefficients.
Nonlinear	Non-parametric methods	KNN	A non-parametric method that predicts a target value based on the average (or weighted average) of its k-nearest neighbors.
	Kernel-based methods	GP	A Bayesian regression method that models the distribution over functions, providing uncertainty estimates in predictions. Matern Kernel is used.
		KRR	Combines Ridge Regression with kernel methods (radial basis functions) to capture non-linear relationships in data.
		SVR	A regression technique using Support Vector Machines, aiming to find a hyperplane that best fits the data within a margin.
	Tree-ensemble methods	ETR	Similar to Random Forest but introduces more randomness in tree splits to reduce variance further.
		XGB	A powerful gradient boosting algorithm that optimizes decision trees to maximize accuracy and efficiency.
		RFR	Uses an ensemble of decision trees to improve prediction accuracy and reduce variance through bagging.

Supplementary Table 6. Hyperparameter search ranges (with all other parameters set to the default values in Scikit-learn, unless otherwise stated).

Method	Hyperparameters
Lasso	$\alpha \in [10^{-2}, 10^{-1}, 1.0, 10^{1}, 10^{2}]$
Ridge	$\alpha \in [10^{-2}, 10^{-1}, 1.0, 10^{1}, 10^{2}]$
KNN	n_neighbors $\in [2, 4, 8, 16], p \in [2, 3]$
GP	$Kernel = Matern5/2, , \alpha = 10^{-10}$
KRR	$\alpha \in [10^{-5}, 10^{-4}, 10^{-3}, 10^{-1}, 1.0]$, $\gamma \in [10^{-5}, 10^{-4}, 10^{-3}, 10^{-1}, 1.0]$
SVR	kernel='rbf', $C \in [1.0, 10^{1}, 10^{2}, \cdots, 10^{5}]$, $\gamma \in [1.0, 10^{-1}, 10^{-2}, \cdots, 10^{-10}]$, $\epsilon \in [10^{-2}, 10^{-1}, 1.0, 10^{1}, 10^{2}]$
ETR	n_estimator=200, max_features $\in [sqrt, 1.0]$, min_samples_leaf $\in [1, 2, 5, 10]$, max_leaf_node $\in [None, 70]$, bootstrap $\in [True, False]$
XGB	n_estimator=200, max_depth $\in [6, 7, 8]$, learning_rate $\in [0.1, 0.05]$, subsample $\in [0.8, 0.9, 1]$, colsample_bytree $\in [0.8, 0.9, 1]$
RFR	n_estimator=200, max_features $\in [sqrt, 1.0]$, min_samples_leaf $\in [1, 2, 5, 10]$, max_leaf_node $\in [None, 70]$

Supplementary Table 7. (separate file) Formulations of hydrogels derived from machine learning (ML) predictions, along with their swelling properties in normal saline (0.154 M NaCl). Columns include: **s**ample index, monomer proportions (ϕ_i), adhesive strength (F_a) measured by tack test on a glass substrate with a 10 N loading force and 10-second contact time, hydrogel thickness (d), and volume swelling ratio (Q). The top-performing gels in each ML round are highlighted in bold.

Supplementary Table 8. Formulations, volume swelling ratios (Q), Young's modulus (E), storage modulus (G') at a frequency of 10^0 rad s^{-1}, and adhesive strength (F_a) of the top-performing hydrogels from data mining and three machine learning optimization rounds. Tack tests were conducted under a 20 N loading force applied for 60 seconds on a glass substrate in normal saline (0.154 M NaCl). All hydrogels were equilibrated in normal saline.

No.	Φ_{HEA}	Φ_{BA}	Φ_{CBEA}	Φ_{ATAC}	Φ_{PEA}	Φ_{AAm}	*Q*	*E (kPa)*	*G′ (kPa)*	*F_a (MPa)*
G-max	0.141	0.591	0.076	0.096	0.096	0.000	0.42±0.04	125.60±5.74	5.86	0.50±0.02
R1-max	0.000	0.588	0.000	0.094	0.318	0.000	0.51±0.06	320.76±7.93	18.72	1.02±0.01
R2-max	0.000	0.629	0.000	0.061	0.310	0.000	0.42±0.02	459.99±26.74	24.69	0.85±0.04
R3-max	0.000	0.680	0.000	0.070	0.250	0.000	0.50±0.04	538.95±4.72	25.35	0.86±0.01

Supplementary Video 1. Demonstration of the mechanical properties of R1-max and R2-max hydrogels under stretching and puncture resistance tests. The video highlights their high stretchability and strong resistance to puncture (linked to Fig. 5c).

Supplementary Video 2. Demonstration of R1-max hydrogel used to adhere a rubber duck to a rock in the sea. The video highlights the hydrogel's strong adhesion in saltwater, enabling the duck to withstand continuous ocean tides and wave impacts (linked to Extended Data Fig. 10a).

Supplementary Video 3. Demonstration of using R2-max hydrogel to stop a burst of tap water from a damaged pipe. The video highlights the hydrogel's effectiveness in sealing a 20-mm hole at the base of a 3-meter-tall polycarbonate pipe filled with tap water. Upon application, R2-max instantly halted the high-pressure water leak, showcasing its rapid sealing capability (linked to Extended Data Fig. 10b).

Supplementary Data 1. (separate file) Consensus sequence fragments of proteins from the top 200 species.

Supplementary Data 2. (separate file) Pairwise functional class counting within consensus sequence fragments of proteins from the top 200 species.

References

52 Koltzenburg, S., Maskos, M. & Nuyken, O. Polymer Chemistry. *Springer* (2017).

53 Long, R. & Hui, C.-Y. Fracture toughness of hydrogels: measurement and interpretation. *Soft Matter* **12**, 8069-8086 (2016).

54 Cedano-Serrano, F. J. *et al.* From molecular electrostatic interactions and hydrogel architecture to macroscopic underwater adherence. *Macromolecules* **52**, 3852-3862 (2019).

55 Qiao, H. *et al.* Multiple weak h-bonds lead to highly sensitive, stretchable, self-adhesive, and self-healing ionic sensors. *ACS Appl. Mater. Interfaces* **11**, 7755-7763 (2019).

56 Fan, H. L., Wang, J. H. & Gong, J. P. Barnacle cement proteins-inspired tough hydrogels with robust, long-lasting, and repeatable underwater adhesion. *Adv. Funct. Mater.* **31**, 2009334 (2021).

57 Liu, X., Zhang, Q. & Gao, G. DNA-inspired anti-freezing wet-adhesion and tough hydrogel for sweaty skin sensor. *Chem. Eng. J.* **394**, 124898 (2020).

58 Fan, X. *et al.* An antifreezing/antiheating hydrogel containing catechol derivative urushiol for strong wet adhesion to various substrates. *ACS Appl. Mater. Interfaces* **12**, 32031-32040 (2020).

59 Han, L., Wang, M., Prieto-López, L. O., Deng, X. & Cui, J. Self-hydrophobization in a dynamic hydrogel for creating nonspecific repeatable underwater adhesion. *Adv. Funct. Mater.* **30**, 1907064 (2020).

60 Wang, S. *et al.* Ultrasonic-induced synthesis of underwater adhesive and antiswelling hydrogel for strain sensor. *ACS Appl. Mater. Interfaces* **14**, 50256-50265 (2022).

61 Fu, C. *et al.* Hydrogel with robust adhesion in various liquid environments by electrostatic induced hydrophilic and hydrophobic polymer chains migration and rearrangement. *Adv. Mater.* **35**, 2211237 (2023).

62 Wang, Z. *et al.* Robust underwater adhesives based on dynamic hydrophilic and hydrophobic moieties to diverse surfaces. *ACS Appl. Mater. Interfaces* **13**, 3435–3444 (2021).

63 Wei, X. *et al.* Underwater adhesive HPMC/SiW-PDMAEMA/Fe3+ hydrogel with self-healing, conductive, and reversible adhesive properties. *ACS Appl. Polym. Mater.* **3**, 837–846 (2021).

64 Chen, K. *et al.* An all-in-one tannic acid-containing hydrogel adhesive with high toughness, notch insensitivity, self-healability, tailorable topography, and strong, instant, and on-demand underwater adhesion. *ACS Appl. Mater. Interfaces* **13**, 9748–9761 (2021).

65 Lee, J. N., Lee, S. Y. & Park, W. H. Bioinspired self-healable polyallylamine-based hydrogels for wet adhesion: synergistic contributions of catechol-amino functionalities and nanosilicate. *ACS Appl. Mater. Interfaces* **13**, 18324–18337 (2021).

66 Rao, P. *et al.* Tough hydrogels with fast, strong, and reversible underwater adhesion based on a multiscale design. *Adv. Mater.* **30**, 1801884 (2018).

67 He, S. *et al.* Bio-inspired instant underwater adhesive hydrogel sensors. *ACS Appl. Mater. Interfaces* **14**, 45869-45879 (2022).

68 Han, I. K. *et al.* Electroconductive, adhesive, non-swelling, and viscoelastic hydrogels for bioelectronics. *Adv. Mater.* **35**, 2203431 (2022).

69 Xu, W. *et al.* Synergy of host–guest and cation−π interactions for an ultrastretchable, ph-tunable, surface-adaptive, and salt-resistant hydrogel adhesive. *Chem. Mater.* **34**, 8740-8748 (2022).

70 Huang, G. *et al.* Tough hydrophobic hydrogels for monitoring human moderate motions in both air and underwater environments. *Chem. Mater.* **35**, 5953-5962 (2023).

71 Ming, X. *et al.* Isopropanol-regulated adhesion-controllable conductive gels for robust bioelectric signal monitoring and flexible underwater robots. *Chem. Eng. J.* **460**, 141746 (2023).

72 Zhang, Z., Guo, L. & Hao, J. Emulsion-based organohydrogels with switchable wettability and underwater adhesion toward durable and ecofriendly marine antifouling coatings. *ACS Appl. Polym. Mater.* **3**, 3060–3070 (2021).

73 Chang, M. *et al.* A highly stretchable, UV resistant and underwater adhesive hydrogel based on xylan derivative for sensing. *Int. J. Biol. Macromol.* **220**, 1084-1094 (2022).

74 Li, M. *et al.* Water-induced phase separation for anti-swelling hydrogel adhesives in underwater soft electronics. *Adv. Sci.* **10**, 2304780 (2023).

75 Sun, C. *et al.* Water-resistant and underwater adhesive ion-conducting gel for motion-robust bioelectric monitoring. *Chem. Eng. J.* **431**, 134012 (2022).

76 Du, P., Wang, J., Hsu, Y.-I. & Uyama, H. Hydrophobic association hydrogel enabled by multiple noncovalent interactions for wearable bioelectronics in amphibious environments. *Chem. Mater.* **36**, 1318-1332 (2024).

77 Ye, B. *et al.* Glycopolymer-based antiswelling, conductive, and underwater adhesive hydrogels for flexible strain sensor application. *ACS Biomater. Sci. Eng.* **9**, 6891-6901 (2023).

78 Yang, H. *et al.* Reversible, ultra-strong underwater adhesive based on supramolecular interaction for instant liquid leakage sealing and robust tissue adhesion. *Chem. Eng. J.* **480**, 148064 (2024).

79 Zhao, G. *et al.* Barnacle inspired strategy combined with solvent exchange for enhancing wet adhesion of hydrogels to promote seawater-immersed wound healing. *Bioactive Materials* **41**, 46-60 (2024).

80 Beharaj, A., McCaslin, E. Z., Blessing, W. A. & Grinstaff, M. W. Sustainable polycarbonate adhesives for dry and aqueous conditions with thermoresponsive properties. *Nat. Commun.* **10**, 5478 (2019).

81 Wang, Y.-J. *et al.* Polymer pressure-sensitive adhesive with a temperature-insensitive loss factor operating under water and oil. *Adv. Funct. Mater.* **31**, 2104296 (2021).

82 Wang, Z. *et al.* Polymer network editing of elastomers for robust underwater adhesion and tough bonding to diverse surfaces. *ACS Appl. Mater. Interfaces* **13**, 36527–36537 (2021).

83 Zhou, Y. *et al.* Pressure-sensitive adhesive with enhanced and phototunable underwater adhesion. *ACS Appl. Mater. Interfaces* **13**, 50451-50460 (2021).

84 Niu, W., Zhu, J., Zhang, W. & Liu, X. Simply formulated dry pressure-sensitive adhesives for substrate-independent underwater adhesion. *ACS Mater. Lett.* **4**, 410-417 (2022).

85 Wu, Y. *et al.* Photo-curing preparation of biobased underwater adhesives with hydrophobic chain-ring interlace structure for protecting adhesion. *Appl. Mater. Today* **27**, 101436 (2022).

86 Wu, Y. *et al.* A photocured bio-based shape memory thermoplastics for reversible wet adhesion. *Chem. Eng. J.* **470**, 144226 (2023).

87 Zhang, Y. *et al.* Super-tough and fast adhesion of soft elastomer based on strong

noncovalent interaction in diverse environments. *Adv. Funct. Mater.* **33**, 2304653 (2023).

88 Kaymazlar, E., Andac, O. & Garcia, S. J. Water-triggered self-healing and reversible underwater adhesion in metalorganic polymers. *J. Mater. Chem. A* **12**, 18338-18347 (2024).